

EARLY CAREER SCHOLARS IN MATERIALS SCIENCE

Hot deformation and softening response in boron-modified two-phase titanium aluminide Ti-48Al-2V-0.2B

Nitish Bibhanshu^{a),†} , Gyan Shankar, Satyam Suwas^{b)}

Department of Materials Engineering, Indian Institute of Science Bangalore, Bangalore 560012, India

a) Address all correspondence to these authors. e-mail: nitishb@iisc.ac.in, nitishbibhanshu@gmail.com

b) e-mail: satyamsuwas@iisc.ac.in

† Current Address: Reactor & Nuclear Systems Division, Oak Ridge National Laboratory, Oak Ridge, TN - 37831, US

Received: 31 May 2020; accepted: 15 September 2020; published online: 1 February 2021

Hot deformation and softening response for the titanium aluminide Ti-48Al-2V-0.2B has been investigated. The deformation response to softening mechanisms has been examined. Deformation experiments were carried out in the strain rate range $0.01\text{--}10\text{ s}^{-1}$ keeping the temperature constant at $1200\text{ }^{\circ}\text{C}$ and in the temperature range $1000\text{--}1200\text{ }^{\circ}\text{C}$ at the strain rate 1 s^{-1} . With an increase in strain rate, the microstructural changes associated with the softening mechanism include breaking of the lamellae, spheroidization of the broken laths and dynamic recrystallization. For the strain rate 1 s^{-1} , deformation in the $(\alpha_2 + \gamma)$ phase field leads to fine recrystallized grains, remnant lamellae and cavitation along the grain boundaries (for temperatures 1000 and $1100\text{ }^{\circ}\text{C}$). Deformation in the $(\alpha + \gamma)$ phase field leads to dynamic recrystallization at the shear bands, within the lamellae, breaking and rotation of the α phase during the continuous increase in the deformation strain.



Nitish Bibhanshu received his bachelor's degree in Metallurgy and Materials Engineering from National Institute of Foundry and Forge Technology, and master and doctoral degrees in Materials Engineering from the Indian Institute of Science Bangalore, India. During the education, he did investigation on processing of several alloys of γ -titanium aluminides and established the relationships between microstructure, texture, mechanical properties. He has also investigated microstructure - mechanical property relations in high entropy alloys, steels, magnesium, and titanium alloys. He was Institute Postdoctoral Research Associate for 6 months at the Indian Institute of Science Bangalore before joining Oak Ridge National Laboratory as a Postdoctoral Research Associate, where he is doing *in situ* experiments to study the mechanical properties of materials.

Introduction

Intermetallics based on γ -titanium aluminide (γ -TiAl) with two different ordered phases α_2 and γ (DO_{19} and L1_0) have been found to be a potential candidate for high-temperature applications. These alloys show a unique combination of properties, such as high specific strength, low density, high fatigue resistance and excellent oxidation resistance [1, 2, 3]. These properties make these alloys amenable for application in place of Ni-based superalloys. However, in titanium aluminides, the constituent phases possess an ordered crystal structure at room temperature which leads to the low plasticity that limits its applications [4]. A number of researchers have proposed that γ -TiAl-based alloys of engineering interest have a composition in which aluminum (Al) is in the range

of 42–49 at.% [5]. Further, the addition of ternary or quaternary alloying elements like V, Nb, Cr, Mn, Si and Mo can enhance plasticity, as well as strength [6, 7, 8]. Boron (B) is a well-known element used for grain refinement in several engineering materials [9]; in the two-phase γ -TiAl alloys, it plays the additional role of stabilizing the α/α_2 phase [10].

A variety of microstructures have been reported for titanium aluminides by modifying the chemistry, as well as by following different thermo-mechanical treatments. Among the several factors, it is well known that equiaxed and duplex structures show a good combination of strength and ductility [11]. Further, it is well established that by appropriate choice of processing parameters, the material can be processed with adequate control over

microstructural evolution that would lead to the above-mentioned features [12, 13, 14].

In order to establish the conditions for obtaining desirable microstructures, a comprehensive understanding of the conditions that would lead to dynamic recrystallization is solicited. Hot compression tests are useful in determining the resistance of the material to plastic deformation for the range of temperatures and strain rates, and they also reveal the conditions for the initiation of dynamic recrystallization. Since the intermetallic γ -TiAl undergoes a number of phase transformations including the ordered-disordered phase transformation for the different constituent phases ($\alpha_2 \leftrightarrow \alpha$, $B2 \leftrightarrow \beta$), it is important to account for all these temperatures in designing the processing strategy for this material. While the transformations like $\beta/\alpha \rightarrow \alpha + \beta \rightarrow \alpha_2 + \beta$ (or B2) decide the nucleation and growth of phases, hence the evolution of the microstructure, the order-disorder transformation temperature (like α_2 to α) plays a crucial role for controlling the plasticity by affecting dislocation and twin activity [15].

In order to impart adequate plasticity and to improve the formability, one of the approaches involves adding a sufficient amount of a β stabilizing element that would promote solidification from liquid to the β phase and reduce the intensity of the otherwise strong α solidification texture. However, the effect of such alloying addition also manifests in further processing. Generally, niobium (Nb), vanadium (V) and molybdenum (Mo) are the most favored alloying additions to titanium aluminides. Effect of V addition on the deformation behavior of alloys has been studied by Whang and Hahn [16]. Hall and Huang [17] reported that the addition of 3 at.% V to the binary alloys Ti-48Al (at.%) and Ti-52Al (at.%) imparts plasticity to some extent. Chaudhari and Das [18] have studied the deformation behavior of Ti-52Al-3V (at.%) alloy and concluded that the addition of 3 at.% V does not change the initial microstructure but affects the microstructural features after deformation. As mentioned earlier [9] that with the addition of a small amount of boron (B) refines the microstructure and also stabilizes the α - phase, which eventually leads to the enhancement in plasticity by promoting twin formation at the interface of the α and γ lamellae.

The present investigation was aimed at examining the mechanism of deformation and softening, in titanium aluminides containing V and B by a detailed microstructural investigation. Two “V” containing compositions, one without and the other with “B” addition have been investigated, namely Ti-48Al-2V and Ti-48Al-2V-0.2B, the former being a control material. Based on the softening response of the two alloys, detailed analyses have been carried out in the ordered and disordered domain of α -phase, and the role of order-disorder transformation has been elucidated.

Results

Microstructural features prior to deformation

The columnar region of as-cast ingot consists of dendritic features and inside the dendrite, lamellae are observed. Both the alloys Ti-48Al-2V and Ti-48Al-2V-0.2B show the lamellar features consisting of α_2 - γ and γ - γ lamellae (in the dendritic arms), as well as some grains of γ -phase distributed along the interface of dendritic arms [Figs. 1(a) and 1(b)]. The percentage for both the phases in inter-dendritic regions, as well as in the colonies, is given in Table 1. The size of the dendritic arms is larger for the Ti-48Al-2V alloys compared to the B-modified alloy. The dendritic arms show the 4-fold symmetry [Figs. 1(a) and 1(b)] which is probably the indication of solidification starting from the cubic crystal structure, that is the β phase.

Prior to deformation, microstructural features were recorded for the samples just water quenched from 1200 °C. The microstructures are displayed in Figs. 1(c) and 1(d). The microstructural features of quenched samples comprise of relatively finer lamellae for the alloy Ti-48Al-2V-0.2B along with some γ phase along the colony's boundaries. The image quality (IQ) map generated from the electron back-scattered diffraction (EBSD) is presented in Fig. 2. The microstructure of Ti-48Al-2V-0.2B shows a larger fraction of γ -grains compared to that of the Ti-48Al-2V alloy. The distribution of γ -phase (phase fraction ~ 22%) has been observed along the interface of the colonies in B-modified composition.

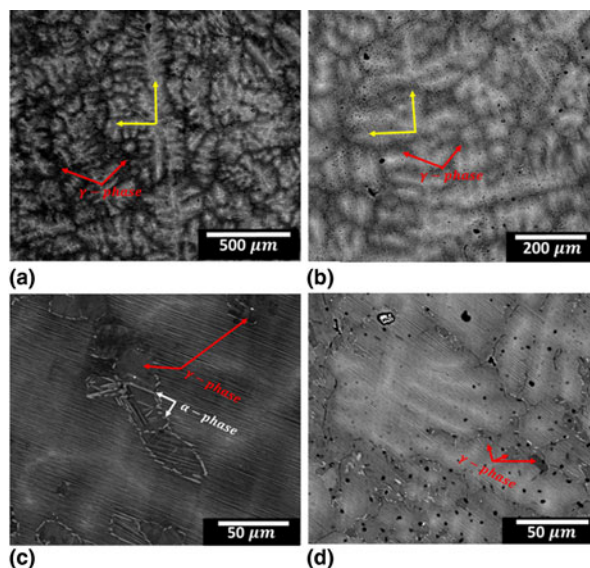


Figure 1: Back-scattered electron micrographs for the as-cast alloy (a) Ti-48Al-2V (As-cast), (b) Ti-48Al-2V-0.2B (As-cast) and water quenched samples from the temperature of 1200 °C presented in (c) Ti-48Al-2V (WQ), (d) Ti-48Al-2V-0.2B (WQ).

TABLE 1: Calculated phase percentage from the back-scattered electron micrographs using ImageJ software in the inter-dendritic regions and colonies for Ti-48Al-2V and Ti-48Al-2V-0.2B alloys (for the cast sample).

Feature/phases	Ti-48Al-2V	Ti-48Al-2V-0.2B	
γ -phase (TiAl)	19.20%	21.40%	
Colonies fraction,	80.80%	54% ($\pm 3.5\%$)	61% α_2
α_2 - γ and γ - γ	1.45 μm	Ti ₃ Al(α_2 -phase)	0.72 μm (\pm phase)
lamellae size	($\pm 0.62 \mu\text{m}$)	46% ($\pm 3\%$)	0.32 (μm)
		TiAl(γ -phase)	39% γ phase

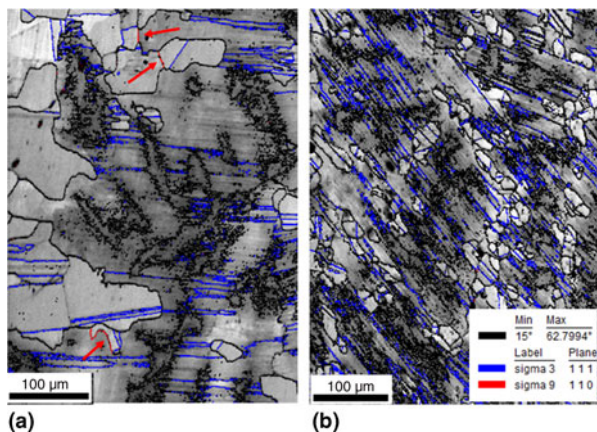


Figure 2: Image quality map generated from EBSD with superimposed $\Sigma 3$, $\Sigma 9$ and random boundary for water quench samples from 1200 °C for the alloys (a) Ti-48Al-2V and (b) Ti-48Al-2V-0.2B.

Oxidation behavior in argon (Ar) atmosphere

High-temperature treatment in the argon atmosphere can also lead to the oxygen absorption and hence could influence phase stability to some extent. The TGA plot displayed in Fig. 3 clearly indicates the percentage mass gain with the increase in the α transus temperature for both the alloys. It is clear that the rate of mass gain rate is about the same for both alloys up to a temperature of 900 °C. Above this temperature, the rate of mass gain is faster for Ti-48Al-2V. On the other hand, the increase of mass for the B-modified alloy shows a linear increasing trend up to the temperature 1300 °C. Beyond this temperature, the curve indicates a drastic increase of the mass for the boron-modified alloy. The boron-modified alloy shows a higher thermal stability towards oxidation.

Deformation and softening in Ti-48Al-2V and Ti-48Al-2V-0.2B

The stress-strain curves for both alloys deformed at 1200 °C with the strain rate 10 s⁻¹ are presented in Fig. 4(a). A larger drop in flow stress is observed for the alloy Ti-48Al-2V-0.2B [Figs. 4(a) and 4(b)]. Corresponding to a common deformation condition, the BSE micrographs for Ti-48Al-2V and

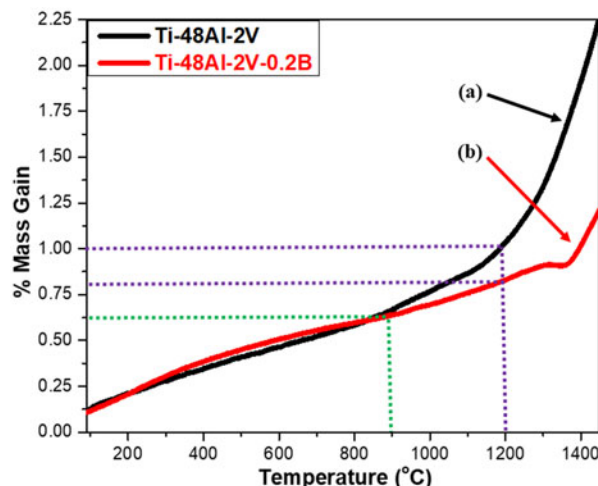


Figure 3: TGA curves depicting the mass gain at the heating rate of 10°/min and in the argon atmosphere at the pressure of 10 torr for the alloys (a) Ti-48Al-2V and (b) Ti-48Al-2V-0.2B.

Ti-48Al-2V-0.2B alloys are presented in Figs. 4(d) and 4(e), respectively. The micrograph of B-modified alloy shows a higher fraction of dynamically recrystallized grains with relatively smaller grain size.

Microstructure of Ti-48Al-2V alloys shows a significant amount of recrystallization in shear bands. The broken and aggregated lamellae of α_2 phase are also observed along the edges of the bands. A detailed orientation analysis of the deformed Ti-48Al-2V alloy (1200 °C and 10 s⁻¹) has been carried out based on the data generated from EBSD. The IPF map of the γ -phase reveals that most of the recrystallization has taken place along the grain boundaries. The IPF map for both the phases at low magnification as well as high magnification is presented in Fig. 5. Along with the larger area scans, a small area scan with the step size of 50 nm has been carried out, and the corresponding IPF maps for both the phases are shown in Figs. 5(d) and 5(e). The IPF maps indicate that some of the γ - γ lamellae are in twin relation.

The B-modified alloy Ti-48Al-2V-0.2B shows a higher degree of dynamic recrystallization for the deformation at the temperature 1200 °C and strain rate 10 s⁻¹. A montage generated from the back-scattered electron (BSE) micrographs of the half-sectioned plane parallel to the compression direction is depicted in Fig. 6. Along the diagonal in the montage, a brighter region is clearly discernible at about 45° with respect to compression direction which is probably the plane of shear [Fig. 6(a)]. For detailed information about microstructural evolution during the deformation, SEM micrographs were recorded at higher magnification at three different locations, as shown in Figs. 6(b) and 6(d). At different locations, microstructural features are different, which is an indication of the change in the state of stress at different locations of

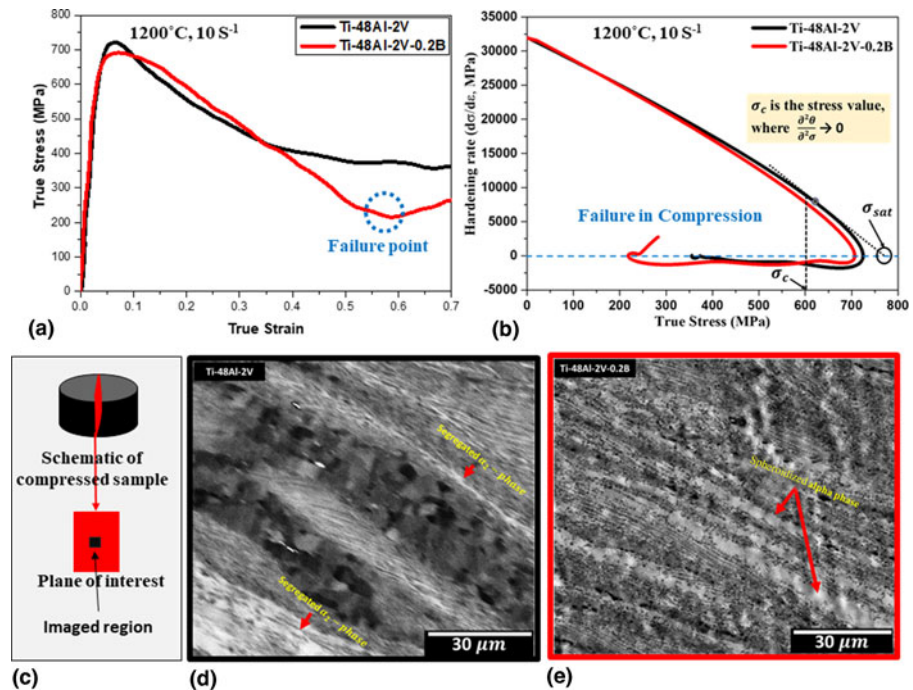


Figure 4: (a) Stress–strain curve obtained from Gleeble, (b) hardening rate as a function of true stress, (c) schematic, depicting compressed sample and imaged region on the plane of interest, (d) back-scattered electron micrograph of Ti–48Al–2V and (e) back-scattered electron micrograph of Ti–48Al–2V–0.2B.

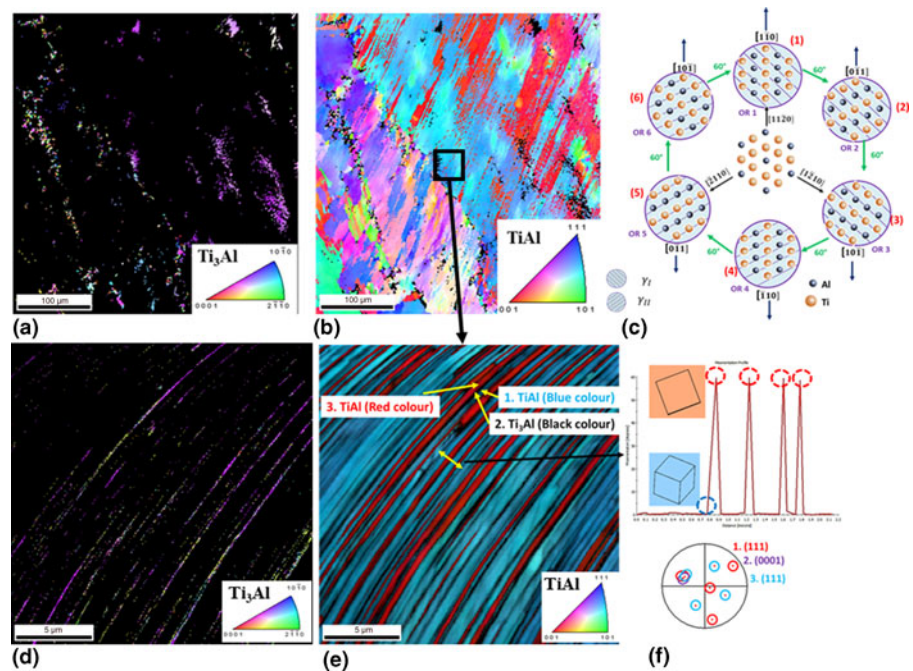


Figure 5: IPF map of TiAl (a,d) and Ti₃Al (b,e) phase of composition Ti–48Al–2V, deformed at 1200 °C and strain rate 10 s⁻¹, (c) atomic orientation relationship for the phase transformation and twin formation (modified of [1]) and (f) misorientation profile of the twin formation.

the deforming sample. Fig. 6(b) shows the presence of spheroidized α_2 phase, as well as dynamically recrystallized γ -phase, in the shear bands. The gap between two consecutive bands is separated by the spheroidized grains of α_2 phase. At the central location, a very fine DRX grain appears [Fig. 6(c)]. The microstructure at a distance from the shear plane [Fig. 6(d)] displays the kinked lamellae with a kinking direction parallel

to the direction of the shear band. This indicates that prior to the formation of shear band, kinking of the lamellae takes place.

Having ensured that the degree of softening in Ti–48Al–2V–0.2B alloy is much higher, this material was subjected to a detailed study of deformation behavior in a range of temperature and strain rates.

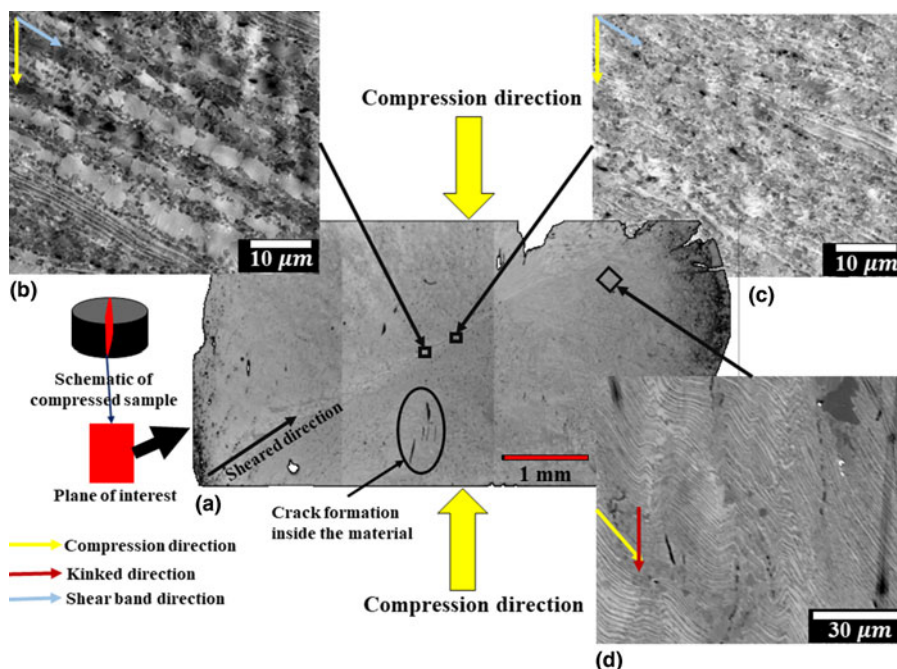


Figure 6: Back-scattered electron micrograph at different locations of the deformed B-modified alloy (Ti-48Al-2V-0.2B) at 1200 °C and 10 s⁻¹. (a) Montage of complete half-sectioned plane, (b) at the shear plane but little off from the central location, (c) at the central location and (d) near the edge and little off from the shear plane.

Stress-strain response and activation energy of deformation

Stress-strain curves for the B-modified alloy Ti-48Al-2V-0.2B, deformed at 1 s⁻¹ and for the temperatures of 1000, 1100, 1150 and 1200 °C are shown in Fig. 7(a). For deformation at different strain rates, namely 0.01, 0.1, 1.0, 10.0 s⁻¹ and at the temperature 1200 °C, the stress-strain curves are presented in Fig. 7(b). The curves display four distinct regions: elastic (region - I), hardening (region - II), softening (region - III) and saturation of flow stress (region - IV). A larger range of strain is covered by the region - III. In this domain, the flow stress decreases with an increase of strain. Higher drop in the stress is because of higher softening during the deformation. For the deformation at 1000 and 1100 °C, flow stress shows the same trend. Similarly, for deformation at 1175 and 1200 °C, the curves are alike. The stress-strain curves indicate the trend of a decrease in the peak and flow stresses with decrease in the strain rate.

It is well known that the strain rate, temperature, peak stress, strain rate sensitivity and activation energy of deformation are connected by the following equation [19].

$$\dot{\epsilon} = A\sigma_p^{1/m} \exp\left(\frac{-Q}{RT}\right) \quad (1)$$

where A is a constant, R is a gas constant, and $\dot{\epsilon}$, T , σ_p , m and Q are strain rate, temperature, peak stress, strain rate sensitivity and activation energy of deformation, respectively. From Eq. (1), the strain rate sensitivity, as well as the activation energy of deformation, can be derived and expressed by the equations mentioned below. Strain rate

sensitivity is calculated for the constant temperature and strain. However, activation energy of deformation was calculated for a given strain rate.

$$m = \frac{1}{n} = \left(\frac{\partial \ln \sigma_p}{\partial \ln \dot{\epsilon}}\right)_{T,\epsilon} \quad (2)$$

$$Q = \left(\frac{\partial \ln \sigma_p}{\partial \frac{1}{T}}\right)_{\dot{\epsilon}} \cdot \left(\frac{\partial \ln \dot{\epsilon}}{\partial \ln \sigma_p}\right)_T \quad (3)$$

Mathematically, the reciprocal of the strain rate sensitivity is defined as the stress exponent. Strain rate sensitivity, as well as the activation energy of deformation, can be calculated from Eqs. (2) and (3), respectively. The plot of the ln(peak stress) versus ln(strain rate) is shown in Fig. 7(c). The slope of the linear fitting gives the value of m , and reciprocal of m is 5.46 (value of n). The activation energy of deformation was also calculated as a function of temperature and it is observed that its value increases with temperature. As the activation energy of deformation depends on the phase fraction, the variation of the α/α_2 phase fraction was also calculated from the binary phase diagram of Ti-Al for the temperature range of 1000-1200 °C. The measurement was carried out at the identical temperature of deformation. The variation of activation energy and α/α_2 -phase percentage with temperature are also shown in Fig. 7(d).

Deformed microstructure

BSE micrographs of deformed samples are presented in Fig. 8. The micrographs were recorded at an identical location on the

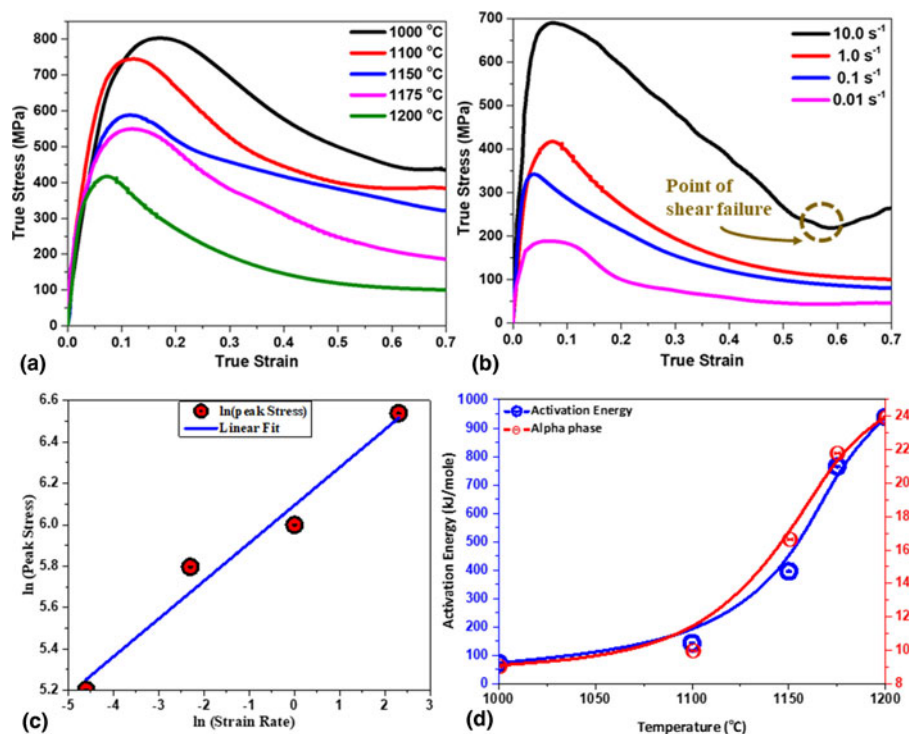


Figure 7: (a) Compression curve at strain rate 1 s^{-1} and different temperatures, (b) compression curve at the temperature $1200 \text{ }^\circ\text{C}$ and different strain rate (c) \ln (Peak stress) versus \ln (Strain rate) plot and (d) activation energy and α_2/α -phase distribution as a function of temperature for range of $1000\text{--}1200 \text{ }^\circ\text{C}$.

half-sectioned equatorial plane. For deformation at 1000 and $1100 \text{ }^\circ\text{C}$, microstructural features are about similar. As, the deformed micrograph for deformation at $1000 \text{ }^\circ\text{C}$ shows very fine recrystallized grains with some cavitation. However, in the localized regions, cracks are at an angle of about 45° with respect to the compression direction [Fig. 8(b)]. However, the micrographs of the sample for deformation at $1100 \text{ }^\circ\text{C}$ shows the broken lamellae and recrystallized grains within it. Along with the broken lamellae, cavities are distributed [Fig. 8(c)]. Further, with an increase in the deformation temperature, the formation of recrystallized grains along with some remnant and aggregated lamellae are observed. In the region of remnant lamellae, some of the recrystallized grains are also observed in the inter-lamellar regions [Figs. 8(c)–8(e)]. For deformation at $1175 \text{ }^\circ\text{C}$, relatively higher fraction, higher recrystallized grains are observed in the micrographs. Along with these recrystallized grains, remnant lamellae with some bending are also indicated. In the remnant lamellar regions, some of the recrystallized grains of the γ phase are observed within it [Fig. 8(e)]. However, for the sample deformed at $1200 \text{ }^\circ\text{C}$ and 1 s^{-1} , microstructural features depict a higher fraction of the dynamically recrystallized grains in the shear band [Fig. 8 (f)]. With this higher fraction of dynamically recrystallized grains, α_2 phase is found to be globularized in the deformed microstructure. For the deformation at $1200 \text{ }^\circ\text{C}$ and 0.01 s^{-1} , the SEM micrograph with a higher aggregated α_2 phase is observed which is shown in Fig. 8(h). The dynamically recrystallized γ -phase as well as broken lamellae which are getting

aggregated are aligned at about 45° with the compression direction.

A detailed analysis at a distance away from the shear planes (location of investigation is shown in the schematic of Fig. 9) for the sample deformed at $1175 \text{ }^\circ\text{C}$ and 1.0 s^{-1} . Most of the dynamically recrystallized grains are distributed along the grain boundary. The phenomena are presented by schematics and corresponding SEM micrographs are shown in Fig. 9. Apart from the colonies boundary, the dynamically recrystallized grains were observed along the interface of the α and γ lamellae. From the micrographs given in Figs. 9(e) and 9(f), it is clear that the DRX grains with higher grain size form along the grain boundaries. The lamellae, which are physically oriented parallel to the grain boundary, also show the recrystallized grains within it. However, the lamellae perpendicular to the grain boundary appears broken and some additional dynamically recrystallized grains are observed.

Discussion

Role of boron on cast microstructure and oxidation

It is well known that the addition of B to Ti-alloys and aluminides leads to the formation of different types of borides, e.g. TiB_2 , TiB and Ti_3B_4 . These borides may form a variety of shapes like particles, plates, flakes and needles. The formation of different shapes of the borides basically depends on the composition of the alloy (percentage of boron and β stabilizing elements) [20, 21, 22]. Borides in the present system (Ti–48Al–

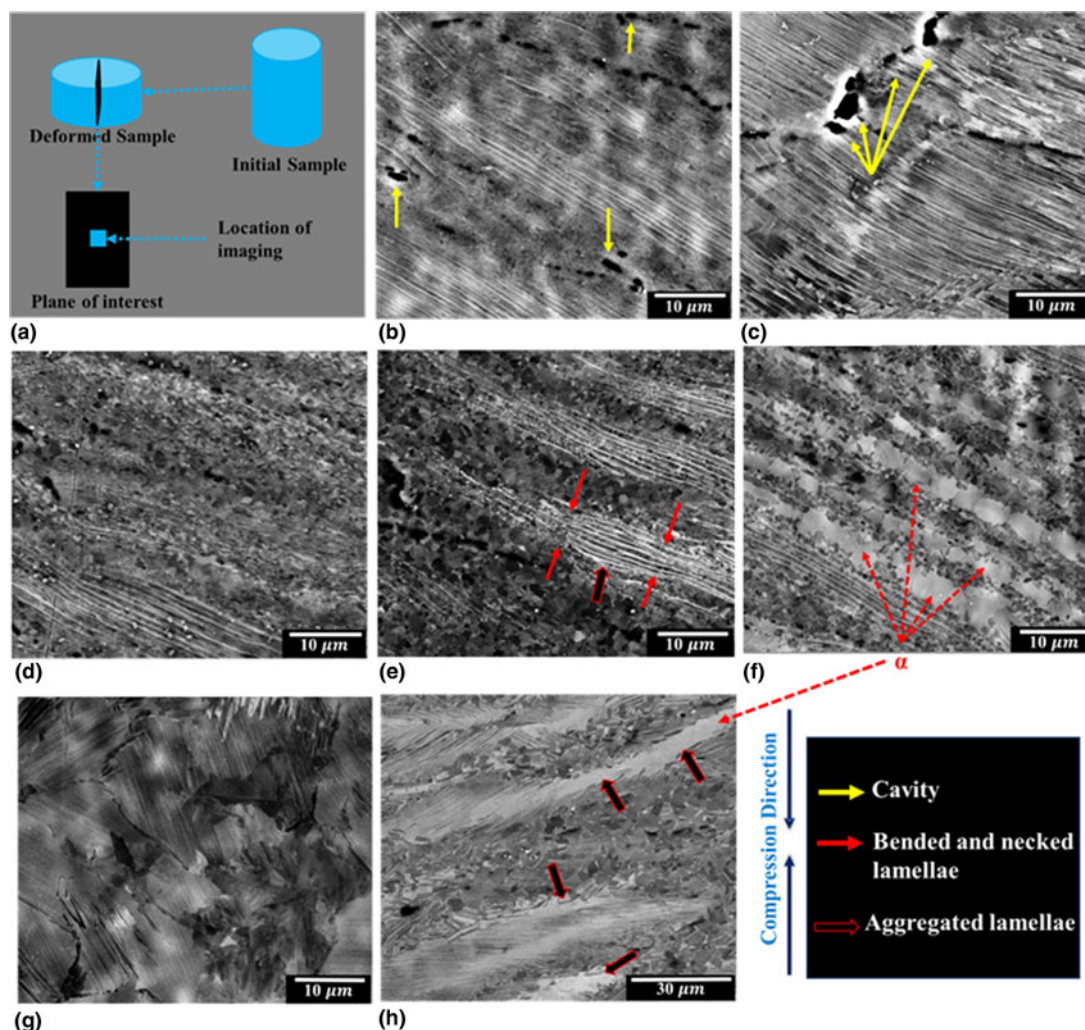


Figure 8: (a) Schematic of imaged regions and back-scattered electron micrograph for the alloy Ti-48Al-2V-0.2B and at the deformation conditions of (b) 1000 °C, 1 s⁻¹; (c) 1150 °C, 1 s⁻¹; (d) 1175 °C, 1 s⁻¹; (e) 1200 °C, 1 s⁻¹; (f) 1200 °C, 10 s⁻¹; (g) 1200 °C, 0.1 s⁻¹ and (h) 1200 °C, 0.01 s⁻¹.

2V-0.2B) are flakes or fine particles of most likely TiB₂ as the B percentage is less than 0.2 at.% [23]. It provides the nucleation sites to start the solidification and also stabilize α phase, which forms during the solidification. Subsequent transformation of this α phase to α_2 causes a higher fraction of α_2 -phase in B-modified alloy (Table 1). Arms of the dendrites are at $\sim 90^\circ$ [Figs. 1(a) and 1(b)], which indicates that solidification starts from a phase that has 4-fold symmetry [23]. The lamellar features in the dendritic arms evolve by the continuous cooling and transformation by following a probable sequence of $L \rightarrow \beta + \alpha \rightarrow \alpha \rightarrow \alpha_2 + \gamma$.

As boron acts as a grain refiner and has the potential to enhance the ordering temperature ($\alpha_2 \rightarrow \alpha$) [24]. The borides in the alloys, as well as boron in the interstitial of α/α_2 phase, cause less diffusivity of oxygen and hence less absorption of oxygen during heating to higher temperature [25]. Oxygen is a stronger α_2/α -phase stabilizer compared to boron, which causes more brittleness and increase in strength for Ti-48Al-

2V alloy as compared to the boron-modified alloy [stress-strain curve in Fig. 4(a)]. Absorption of oxygen in the alloy Ti-48Al-2V-0.2B is lower as compared to the Ti-48Al-2V alloy at a higher temperature (Fig. 3).

Heating the samples to a temperature of 1200 °C shows a different amount of oxygen absorption for both alloys. The alloy Ti-48Al-2V is expected to have the oxygen content as 1000 ppm (1.0 wt%) whereas the B-modified composition has only 800 ppm (0.8 wt%) of oxygen (while Lefevre [26] reported up to 6 at.% [i.e., 25,000 ppm]). With an increase in the solubility of oxygen in the two alloys, strength increases because of the increased stability of α_2 phase. Increasing the α stabilizer content causes a higher thickness of α_2 lamellae and leads to the increase of inter-lamellar spacing. These lamellar interfaces can hinder the dislocations mobility, thereby increase in deformation resistance and higher strength. In conclusion, high oxygen content can be a reason for high strength which is observed in the Ti-48Al-2V alloy. In addition, the

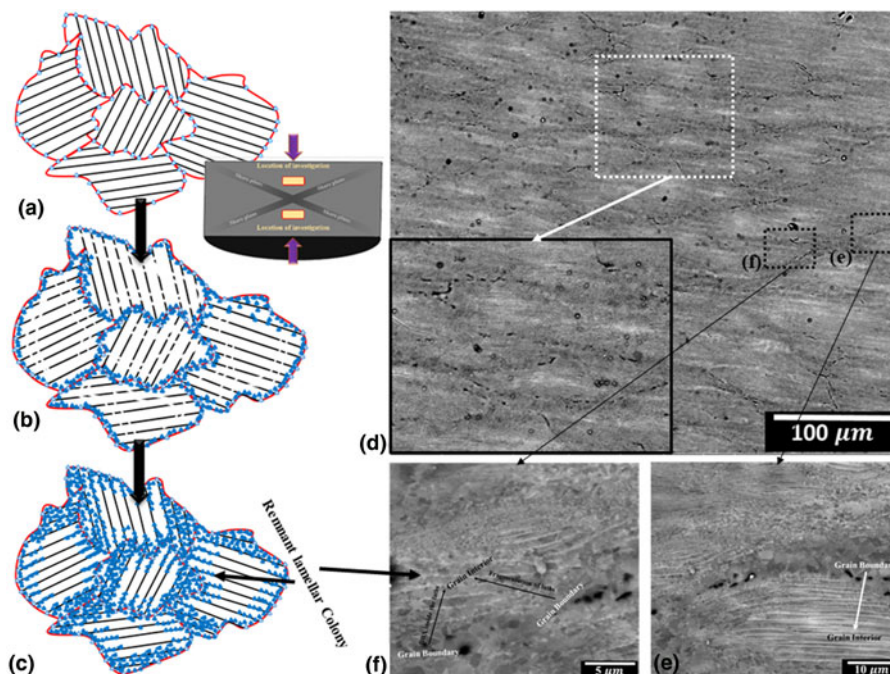


Figure 9: Back-scattered electron micrograph, at the little off location from the shear plane and in the central region, of the sample deformed at 1175 °C and 1 s⁻¹, (a) schematic of initial microstructural features, (b) formation of the DRx grains along the grain boundary breaking of the lamellae whose physical orientation is perpendicular to grain boundary, (c) DRx along the domain of the broken lamellae, (d) micrographs depicting the phenomena of DRx along the grain boundary, (e) and (f) are the magnified micrographs at two locations along the grain boundary.

lesser diffusion of oxygen in the boron-modified alloy leads to the higher plasticity (higher degree of dynamic recrystallization is the representation of higher plasticity) and relatively lower strength compared to the Ti-48Al-2V alloy.

Twin formation

Water quenched samples from 1200 °C exhibit the twin boundary similar to FCC crystal structures (rotation of (111) plane by 60° about [111] direction). This type of boundary is basically joining γ variants which is rotated by an angle of 60°; the $\langle 1\bar{1}0 \rangle$ direction of the matrix is antiparallel to $\langle 10\bar{1} \rangle$ direction [Fig. 5(c)]. In L1₀ structure, $\langle 1\bar{1}0 \rangle$ direction is different from the $\langle 01\bar{1} \rangle$ directions, whereas the three $\langle 11\bar{2}0 \rangle$ directions in the α_2 phase are equivalents. Hence the γ -phase with pseudo-twin boundary nucleates in the six orientation variants, as shown in Fig. 5(c) [27]. In the IPF map of γ -phase, the formation of the twin boundaries is shown in Fig. 5(e). The misorientation angle between the twin boundaries is depicted by line vector, misorientation profile, as well as in the (111) pole figure [Fig. 5(f)]. The percentage of twin boundary was found to be $\sim 18\%$ for the B-modified composition whereas $\sim 15\%$ for Ti-48Al-2V (Fig. 2).

The micrograph of the deformed material shows a true twin boundary which is $\sim 180^\circ$ mis-oriented and pseudo-twin boundary [Fig. 5(e)]. The formation of twin during deformation at a higher temperature was identified to be higher than the pseudo twin. This is possibly connected with its formation during the deformation and the formation of pseudo twin can be related to events pertaining to temperature-dependent

transformation. At constant temperature and strain rate, the deformation-based twin formation activity is relatively higher. The $[1\bar{1}0]$ direction of the matrix is antiparallel to the $[\bar{1}10]$ direction of the twin. At the interface, only the stacking sequence of the parent L1₀ structure is changed. In Fig. 5(c), the variants $[1\bar{1}0]/[\bar{1}10]$, $[0\bar{1}1]/[01\bar{1}]$ and $[10\bar{1}]/[\bar{1}01]$ are related by the true twin. Formation of a different kind of twin boundary is related to the temperature and deformation conditions.

Softening mechanism

Based on the detailed investigation of stress-strain curves, as well as post-mortem characterization of deformed sample, the mechanism of dynamic softening is analyzed. The initial sample has dendritic arms which consist of the lamellar features within. Hot deformation at the desirable temperature leads to softening [28, 29]. In the first step, lamellae undergo kinking and a stress concentration develops at the tip of the lamellae [30]. Higher stress concentration leads to the formation of strain gradient and eventually shear banding [30, 31]. In the second step, due to a high strain gradient because of shear bands, recrystallization in the γ -phase starts and subsequently accelerates with a time of deformation [30]. During unidirectional compression, maximum shear force gets induced at $\sim 45^\circ$ to compression direction [32, 33]. This induced shear forces lead to the formation of the shear band at an angle of $\sim 45^\circ$ [Fig. 6(a)] [33, 34, 35]. At a location little away from the shear band, the microstructural features show the kinked lamellae [Fig. 6(d)]. In the shear band, micrographs show

complete recrystallization [Fig. 6(c)] and messed up microstructural features for the central location. However, away from the central region along the shear band, microstructure has a unique combination of the dynamically recrystallized grains of γ -phase and globularized α_2/α -phase [Fig. 6(b)]. The microstructural variation occurs in the deformed sample because of the induced state of stress which is different at different locations [36]. Different state of stress leads to the different mechanisms of softening and microstructural evolution.

The microstructure evolved after deformation at 1175 °C and strain rate 1 s^{-1} shows the neckless type of features in the deformed Ti-48Al-2V-0.2B alloy. The detailed mechanism for the formation of the necklace structure is represented by the schematics; along with corresponding microstructural features are presented in Fig. 9. The initial microstructural features consist of the distribution of some of the γ -phase along the colonies boundary [in the schematic shown in Fig. 9(a) and in the SEM micrograph of Fig. 1(d)]. Deformation at higher temperatures leads to the formation of the DRX along the colony boundaries which consists of mostly γ -phase. Further, with an increase in strain, the lamellae, with the orientation perpendicular to the prior colonies boundary shows fragmentation and subsequent dynamic recrystallization [Fig. 9(c) and 9(f)]. However, the lamellae, which are parallel to prior boundaries of the colony, are difficult to fragment and hence dynamic recrystallization takes place in the γ -phase [Fig. 9(e) and 9(c)]. The parallel oriented lamellae prior to the colony boundaries can exhibit a higher activity of dislocation, which leads to the higher degree of dynamic recrystallization. For the lamellae oriented perpendicular, the α phase acts as a barrier for the dislocation activity rendering recrystallization difficult. Semiatin et al. [14, 37, 38] has reported that the dislocation activity is very low for the α -phase and hence it is difficult to be recrystallized compared to the γ -phase.

Activation energy and stress exponents

In the present case of the boron-modified alloy, the activation energy of deformation increases with temperature. The activation energy of deformation depends on the crystal structure, phase fraction, microstructural features, as well as the crystallographic texture. In the two-phase region, it is strongly dependent on the phase fraction. From the phase diagram [39], it is clear that with an increase in the temperature, the fraction of α/α_2 phase also increases, as shown in Fig. 7(d). Semiatin et al. [40] suggested that the activation energy of deformation is higher for the α_2/α -phase compared to the γ -phase. The activation energy of deformation, 360 kJ/mole, is close to the activation energy for self-diffusion of Al in γ -TiAl crystal structure [41]. This suggests that the hot deformation of two-phase ($\gamma + \alpha_2/\alpha$) TiAl alloys is mainly controlled by lattice diffusion. The

increase in α_2/α -phase fraction, which is a low symmetry structure, retards the diffusion of Al in the γ -phase, because of the increase in the activation energy from 360 to 950 kJ/mole. Stress exponent value greater than 5 (here 5.46) indicates strong dislocation accumulation in order to form strain-free regions in the highly strained regions like kinked lamellae, shear bands and highly mis-oriented grain boundary through the formation of DRX grains, during the hot deformation process. The activation energy increases from 360 kJ/mole after the deformation temperature increases from 1125 °C, which implies that the diffusion of Al becomes easier in γ -TiAl after the transformation of α_2 (ordered HCP, $D0_{19}$) to the α -phase (disordered HCP).

Conclusions

A detailed analysis of stress-strain curves, microstructural evolution and thermogravimetric analysis (TGA) of the Ti-48Al-2V-0.2B alloy led to the following conclusions:

- (1) Addition of boron leads to higher softening compared to the control material Ti-48Al-2V. Without B-addition, the recrystallization of γ -phase occurs mostly at the shear bands, while in B-modified alloy Ti-48Al-2V-0.2B, in addition to recrystallization along the shear bands, the spheroidization of the α_2/α -phase also takes place along with the recrystallization of γ -phase.
- (2) Addition of B to Ti-48Al-2V retards oxygen ingress. Oxygen, being a strong α_2/α -phase stabilizer, reduces the ductility of titanium aluminides; however, the addition of B to Ti-48Al-2V (leading to the composition Ti-48Al-2V-0.2B) retains the ductility by refining the grain size and also by resisting the oxygen ingress.
- (3) The overall activation energy of deformation increases with an increase in the phase fraction of α phase. This reveals that the α_2/α -phase is a stronger phase compared to the γ -phase.
- (4) Kinking of the lamellae causes the formation of the shear bands, which lead to the formation of the highly strained region during hot deformation and hence the formation of DRX grains takes place in these regions.
- (5) In the regions away from the shear plane (macroscopically formed at 45° in the deformed sample with respect to the compression direction), dynamic recrystallization takes place along the grain boundaries of the γ - γ phase and at the boundary of α_2/α - γ phases. The lamellae oriented perpendicular with respect to the grain boundary lead to the formation of dynamically recrystallized grains. On the other hand, lamellae orientation parallel to the boundary of colonies leads to the recrystallization of the γ -phase within the lamellae. The fraction of recrystallized γ -phase decreases with towards the grain interior.

Materials and methods

Cast pancakes with nominal compositions Ti–48Al–2V and Ti–48Al–2V–0.2B ((hereafter will be referred to as B-modified) were prepared via vacuum arc melting. To ensure the uniform and homogeneous compositional, these alloys were melted five times. From the cast pancake, cylindrical samples with 6 mm diameter and 9 mm height were prepared for the deformation experiments.

The finished cylindrical samples of both the compositions were subjected to deformation using gleeble at 1200 °C and strain rate 10 s⁻¹. Further, after a detailed investigation, the boron-modified alloy was deformed at 1200 °C at the strain rates 0.01, 0.1, 1.0 and 10.0 s⁻¹ to observe the effect of strain rate on deformation behavior. As the increase of deformation temperature can render deformation in disordered phase region, and vice-versa; it can influence the deformation behavior and hence the softening response. Therefore, deformation was carried out at the temperatures 1000, 1100, 1150, 1175 and 1200 °C at 1 s⁻¹. All the deformation experiments were performed on the Gleeble 3800 thermal mechanical simulator. Further, as oxygen is a strong α -phase stabilizer, hence can additionally influence the deformation behavior, the tests were performed in an argon atmosphere at a pressure of 20 torr. Prior to the compression tests, the oxidation behavior of the samples was investigated in the argon atmosphere. Oxygen absorption test has been carried out by the TGA at lower pressure of argon compared to the actual tests, and at a very slow heating rate (10 °C/min) compared to the gleeble machine heating rate (2 °C/s).

The deformed samples were sectioned perpendicular to the compression axis for microstructural analyses. The cut faces were metallographically polished followed by electro-polishing using LECTROPOL-5 (Struers). The electrolyte used for electro-polishing was prepared using 60 mL per-chloric acid, 600 mL methanol and 360 mL butoxy ethanol. Electro-polishing was carried out for 13 s at the voltage of 27 V. Scanning electron micrographs were recorded on the electro-polished surface in BSE mode using the Scanning Electron Microscope (SEM) ESEM Quanta 200 (FEI). For the detailed analysis of the orientation and phase distributions, EBSD was carried out with an EBSD detector attached to the SEM. While most of the EBSD scans were acquired at the step size of 100 nm, for revealing the finer microstructural features, EBSD scans were recorded using the Field-Emission Scanning Electron Microscope (FE-SEM) SIRION (FEI) at the step size of 50 nm.

Acknowledgment

The authors would like to thank the IIT Madras for providing the Gleeble facility and AFMM department of IISc Bangalore for characterization facility. Special Thanks to Mr.

Rangan K of IIT Madras for their assistance to carry out a successful deformations test on the Gleeble.

References

1. F. Appel, J.D.H. Paul, and M. Oehring: Gamma Titanium Aluminide Alloys. *First* (WILEY-VCH Verlag GmbH & Co. KGaA, Germany, 1 (2011)). doi:10.1002/9783527636204.
2. Y.W. Kim: Ordered intermetallic alloys, part III: Gamma titanium aluminides. *Jom* 46, 30 (1994).
3. L. Tretyachenko: Aluminium – titanium – vanadium. *MSI Eureka in Springer Materials* 11A4, 26–53 (2004). doi:10.1007/11008514_4.
4. A. Lasalmonie: Intermetallics: Why is it so difficult to introduce them in gas turbine engines? *Intermetallics* 14, 1123 (2006).
5. Y. Jiang, Y.H. He, N.P. Xu, J. Zou, B.Y. Huang, and C.T. Liu: Effects of the Al content on pore structures of porous Ti–Al alloys. *Intermetallics* 16, 327 (2008).
6. P. Erdely, R. Werner, E. Schwaighofer, H. Clemens, and S. Mayer: In-situ study of the time – temperature-transformation behaviour of a multi-phase intermetallic stabilised TiAl alloy. *Intermetallics* 57, 17 (2015).
7. Y.W. Kim and D.M. Dimiduk: Progress in the understanding of gamma titanium aluminides. *Jom* 43, 40 (1991).
8. D. Hu: Effect of composition on grain refinement in TiAl-based alloys. *Intermetallics* 9, 1037 (2001).
9. M. Oehring, A. Stark, J.D.H. Paul, T. Lippmann, and F. Pyczak: Microstructural refinement of boron containing β -solidifying γ -titanium aluminide alloys. *Mater. Sci. Forum* 706–709, 1089 (2012).
10. M. Oehring, A. Stark, J.D.H. Paul, T. Lippmann, and F. Pyczak: Microstructural refinement of boron-containing β -solidifying γ -titanium aluminide alloys through heat treatments in the phase field. *Intermetallics* 32, 12 (2013).
11. W.F. Cui, C.M. Liu, V. Bauer, and H.J. Christ: Thermomechanical fatigue behaviours of a third generation γ -TiAl based alloy. *Intermetallics* 15, 675 (2007).
12. S.L. Semiatin, B.W. Shanahan, and F. Meisenkothen: Hot rolling of gamma titanium aluminide foil. *Acta Mater.* 58, 4446 (2010).
13. P. Erdely, P. Staron, E. Maawad, N. Schell, J. Klose, S. Mayer, and H. Clemens: Effect of hot rolling and primary annealing on the microstructure and texture of a β -stabilised γ -TiAl based alloy. *Acta Mater.* 126, 145–153 (2017). doi:http://dx.doi.org/10.1016/j.actamat.2016.12.056.
14. S.L. Semiatin and V. Seetharaman: Load-signature analysis for pack rolling of near-gamma titanium aluminide alloys. *Metall. Mater. Trans. A* 25, 2539 (1994).
15. D.S. Xu, H. Wang, R. Yang, and P. Veyssi re: Point defect formation by dislocation reactions in TiAl. *IOP Conf. Ser. Mater. Sci. Eng.* 3, 012024 (2009).

16. S. H. Whang, and Y. D. Hahn. High temperature ordered intermetallic Alloys III, Materials Research Society Symposium Proceedings, Vol 133, edited by C.T. Liu, A.I. Taub, M.S. Stoloff and C.C Koch (Pittsburgh, Pennsylvania: Materials Research Society), P- 687, 1989.
17. E. L. Hall, and S. C. Huang. High Temperature Ordered Intermetallic Alloys III, Materials Research Society Symposium Proceedings, Vol 133, edited by C.T. Liu, A.I. Taub, M.S. Stoloff and C.C Koch (Pittsburgh, Pennsylvania: Materials Research Society), P-693, 1989.
18. K. Chaudhuri and S. Das: Deformation microstructures of Ti-52at %Al-3at%V alloy. *Philos. Mag. Letts* **67**, 143 (1993).
19. V. Seetharaman and S.L. Semiatin: Influence of temperature transients on the hot workability of a two-phase gamma titanium aluminide alloy. *Metall. Mater. Trans. A Phys. Metall. Mater. Sci.* **27A**, 1987 (1996).
20. D. Hu: Effect of boron addition on tensile ductility in lamellar TiAl alloys. *Intermetallics* **10**, 851 (2002).
21. S. Roy, V. Tungala, and S. Suwas: Effect of hypoeutectic boron addition on the beta transus of Ti-6Al-4V alloy. *Metall. Mater. Trans. A Phys. Metall. Mater. Sci.* **42**, 2535 (2011).
22. U. Hecht, V. Witusiewicz, A. Drevermann, and J. Zollinger: Grain refinement by low boron additions in niobium-rich TiAl-based alloys. *Intermetallics* **16**, 969 (2008).
23. M. Sujata, D.H. Sastry, and C. Ramachandra: Microstructural characterization and creep behaviour of as-cast titanium aluminide Ti-48Al-2 V. *Intermetallics* **12**, 691-697 (2004).
24. A.V. Kartavykh, M.V. Gorshenkov, and D.A. Podgorny: Grain refinement mechanism in advanced TiAl boron-alloyed structural intermetallics: The direct observation. *Mater. Lett.* **142**, 294 (2015).
25. S. Roy, S. Suwas, S. Tamirisakandala, R. Srinivasan, and D.B. Miracle: Processing response of boron modified Ti-6Al-4 V alloy in (alpha + beta) working regime. *TMS 2009 138th Annual Meeting and Exhibition*, February 15-19, 3, 63 (2009).
26. W. Lefebvre, A. Menand, A. Loiseau, and D. Blavette : Atom probe study of phase transformations in a Ti-48 at.% Al alloy. *Mater. Sci. Eng. A* **A327**, 40-46 (2002).
27. S. Zghal, S. Naka, and A. Couret: Quantitative TEM analysis of the lamellar microstructure in TiAl based alloys. *Acta Mater.* **45**, 3005 (1997).
28. H. Liu, R. Rong, F. Gao, Y. Liu, Z. Li, and Q. Wang: Hot deformation mechanisms of an as-extruded TiAl alloy with large amount of remnant lamellae. *J. Mater. Eng. Perform.* **26**, 3151 (2017).
29. N. Bibhanshu and S. Suwas: Hot deformation and dynamic recrystallization in titanium aluminide. *Mater. Sci. Forum* **941**, 1391 (2018).
30. N. Bibhanshu and S. Suwas: Mechanism of shear band formation and dynamic softening in a two-phase ($\alpha_2 + \gamma$) titanium aluminide. *J. Mater. Res.* **35**(13), 1635-1646 (2020). doi:https://doi.org/10.1557/jmr.2020.99.
31. N. Bibhanshu, A. Bhattacharjee, and S. Suwas: Hot deformation response of titanium aluminides Ti-45Al-(5, 10)Nb-0.2B-0.2C with pre-conditioned microstructures. *J. Alloys Compd.*, **832**, 154584 (2020). doi:https://doi.org/10.1016/j.jallcom.2020.154584.
32. A. Dey and A. Mukhopadhyay: Nanoindentation of brittle solids (2014).
33. A. Tazuddin, K. Biswas, and N.P. Gurao: Deciphering micro-mechanisms of plastic deformation in a novel single phase fcc-based MnFeCoNiCu high entropy alloy using crystallographic texture. *Mater. Sci. Eng. A* **657**, 224 (2016).
34. M.J. Lai, C.C. Tasan, and D. Raabe: On the mechanism of {332} twinning in metastable β titanium alloys. *Acta Mater.* **111**, 173 (2016).
35. N.D. Stepanov, D.G. Shaystultanov, N.Y. Yurchenko, S.V. Zhrebtsov, A.N. Ladygin, G.A. Salishchev, and M.A. Tikhonovsky: High temperature deformation behavior and dynamic recrystallization in CoCrFeNiMn high entropy alloy. *Mater. Sci. Eng. A* **636**, 188 (2015).
36. S. Roy and S. Suwas: Enhanced superplasticity for ($\alpha + \beta$)-hot rolled Ti-6Al-4V-0.1B alloy by means of dynamic globularization. *Mater. Des.* **58**, 52 (2014).
37. P.D. Nicolaou, and S.L. Semiatin: The knoop-hardness yield locus of an orthorhombic titanium aluminide alloy. *Metall. Mater. Trans. A* **29**, 1763 (1998).
38. S.L. Semiatin, V. Seetharaman, D.M. Dimiduk, and K.H.G. Ashbee: Phase transformation behavior of gamma titanium aluminide alloys during supertransus heat treatment. *Metall. Mater. Trans. A* **92**, 7 (1998).
39. J.C. Schuster and M. Palm: Reassessment of the binary aluminum-titanium phase diagram. *J. Phase Equilibria Diffus.* **27**, 255 (2006).
40. V. Seetharaman and S.L. Semiatin: Plastic-flow and microstructure evolution during hot deformation of a gamma titanium aluminide alloy. *Metall. Mater. Trans. A* **28**, 2309 (1997).
41. L. Cheng, J. Li, B. Tang, H. Kou, and E. Bouzy: Superplastic deformation mechanisms of high Nb containing TiAl alloy with ($\alpha_2 + \gamma$) microstructure. *Intermetallics* **75**, 62-71 (2016).